Coherent Control and Spectroscopy of a Semiconductor Quantum Dot Wigner Molecule

J. Corrigan,[1] J. P. Dodson,[1] H. Ekmel Ercan,[1] J. C. Abadillo-Uriel,[1] Brandur Thorgrimsson,[1] T. J. Knapp,[1]
Nathan Holman,[1] Thomas McJunkin,[1] Samuel F. Neyens,[1] E. R. MacQuarrie,[1] Ryan H. Foote,[1] L. F. Edge,[2]
Mark Friesen,[1] S. N. Coppersmith,[1,3] and M. A. Eriksson[1,*]

[1]*University of Wisconsin, Madison, Wisconsin 53706, USA*
[2]*HRL Laboratories, LLC, 3011 Malibu Canyon Road, Malibu, California 90265, USA*
[3]*University of New South Wales, Sydney, NSW 2052, Australia*

Semiconductor quantum dots containing more than one electron have found wide application in qubits, where they enable readout and enhance polarizability. However, coherent control in such dots has typically been restricted to only the lowest two levels, and such control in the strongly interacting regime has not been realized. Here we report quantum control of eight different transitions in a silicon-based quantum dot. We use qubit readout to perform spectroscopy, revealing a dense set of energy levels with characteristic spacing far smaller than the single-particle energy. By comparing with full configuration interaction calculations, we argue that the dense set of levels arises from Wigner-molecule physics.

Multielectron semiconductor quantum dots have extremely desirable properties for constructing and operating qubits. For single spin qubits, manipulating electrons above closed shells makes electric field driving more effective [1,2], and certain qubits like quantum dot hybrid qubits [3] rely on multiple electrons to define the qubit states. Two-electron eigenstate energies are particularly important, since singlet-triplet splittings allow for Pauli spin-blockade readout [4] used in singlet-triplet qubits [5–7], exchange based qubits [8,9], quantum dot hybrid qubits [3,10], and single spin qubits [11], especially for high temperature operation [1,12,13].

When the characteristic interaction energy between electrons becomes larger than the orbital confinement energy, electronic states develop correlations and localize, forming Wigner molecules [14–23]. Imaging of such localization has been achieved using scanning electronic [24] and near-field optical [25] methods. The lowest-lying excited states in Wigner molecules have been studied using both optical [26,27] and transport spectroscopy [28,29], and the latter method has been used to observe a reduction in symmetric-antisymmetric orbital splittings [30]. While Wigner-type localization is known to reduce the gap between the ground and first orbital excited state, the impact on higher lying states and quantum control of such states has not been observed in experiments.

This Letter reports pulsed microwave coherent control and spectroscopy of an electrostatically confined semiconductor double quantum dot in the Wigner-molecule regime. We report coherent Rabi control of eight transitions ranging in frequency from 3.3 to 8.3 GHz, corresponding to energies far smaller than the single-particle confinement energy. With Ramsey spectroscopy, we map the energy as a function of double-dot detuning for 2 of these transitions. Using full configuration interaction (FCI) calculations, we argue that this dense manifold of states results from strong correlations and Wigner-molecule physics. Time-domain simulations of the Rabi experiments are used to explain the Rabi oscillations as a function of detuning energy. The full set of experimental spectroscopy results can be fit by a simple model consisting of two-electron states in the right quantum dot tunnel coupled to the lowest-lying state in the left dot.

Figure 1(a) describes the quantum dots, which are formed in an undoped Si-SiGe heterostructure with three layers of overlapping gates [31]. Fabrication details can be found in Ref. [32]. While the device can form three dots, we form two dots under gates $P1$ and $P2$, accumulating the rightmost dot as part of the right electron reservoir. We operate the double quantum dot (DQD) with five electrons near the (4,1)-(3,2) anticrossing, as shown schematically in Figs. 1(b)–1(d). Tunnel rates between the two dots and to the reservoirs are set by gates $B1$, $B2$, and $B3$. Charge sensing is measured using a two-stage cryogenic high-electron-mobility transistor amplifier [33] mounted on a separate printed circuit board (PCB) connected to the sample PCB by stainless steel coax.

We initialize at setting I, shown in Fig. 1(b), in the (4,1) ground state, which has a large splitting between the ground and first excited states. We ramp the DQD detuning ε across the interdot transition line to a manipulation point (M) at positive ε, as shown in Fig. 1(c), where we apply microwave pulse sequences. Rabi and detuned-Ramsey pulses at M drive coherent rotations between two-particle states in the right quantum dot while maintaining the (3,2) configuration. To perform readout, we adiabatically ramp
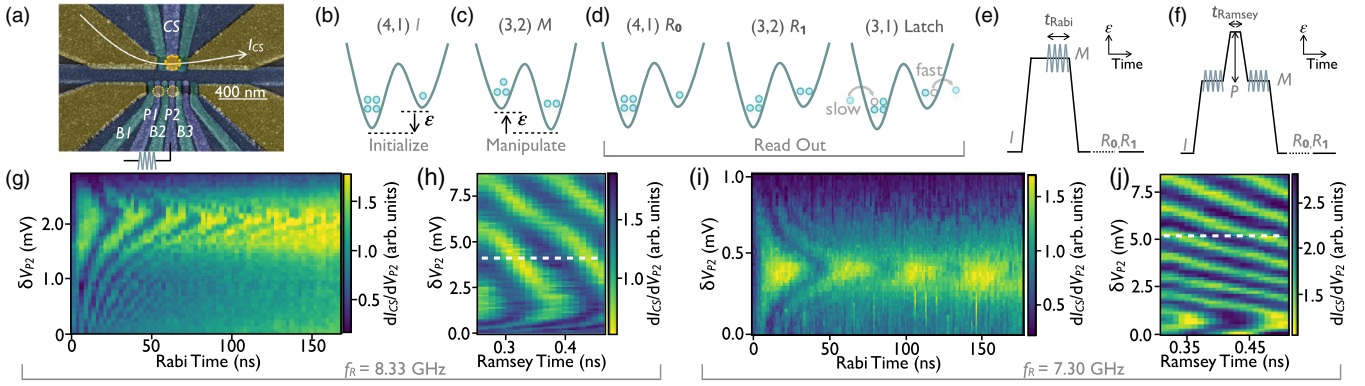
FIG. 1.   (a) False-color micrograph of a device lithographically identical to that measured here. Quantum dots are formed under $P1$ and $P2$. A current I_{CS} flows through the dot controlled by gate CS and is used to detect the electron occupation of the $P1$ and $P2$ dots. (b) The ground state for the five-electron system at negative ε is the charge configuration (4,1), used for initialization (I). (c) The ground state at positive ε is (3,2), used for manipulation (M). (d) Readout of the ground state, R_0, maps onto (4,1), while the excited states, R_1, maintain the (3,2) configuration. The tunnel rates to both reservoirs are tuned for a long decay time from (3,1), enabling latched readout. (e) Rabi pulse sequence used in this work. (f) Ramsey pulse sequence used in this work, composed of two $\pi/2$ pulses and a detuning pulse with amplitude P. (g)–(j) Rabi and detuned-Ramsey measurements of two coexisting states. For (g),(i), δV_{P2} corresponds to a relative shift of the entire pulse sequence; for (h),(j) δV_{P2} corresponds to relative changes in P. Dashed lines in (h),(j) denote the value of δV_{P2} for which $P = 0$. (g),(h) Rabi and Ramsey oscillations using $f_R = 8.33$ GHz. (i),(j) Rabi and Ramsey oscillations using $f_R = 7.30$ GHz, taken at the same device tuning but different ε from (g),(h).

across the interdot transition line: the (3,2) ground state then maps onto the (4,1) ground state (R_0), while the excited states (R_1) maintain their (3,2) configuration, as indicated in Fig. 1(d). Latched measurement [34] is used to enhance readout fidelity: for the excited states (R_1), an electron rapidly tunnels into the right reservoir to form a metastable (3,1) charge state, which slowly returns to the (4,1) ground state. The latch duration is determined by the left barrier, which is tuned to have a long tunnel time.

Figures 1(e)–1(j) demonstrate coherent control of two different DQD transitions performed by applying pulse sequences to gate $P2$ at 8.33 and 7.30 GHz. Fig. 1(e) shows the Rabi sequence, a continuous drive of frequency f_R, and Fig. 1(f) shows the Ramsey sequence, two $\pi/2$ microwave pulses of frequency f_R surrounding a detuning ramp. This Ramsey sequence enables the efficient measurement of energy splittings as a function of ε, and can be performed at any known Rabi resonance location [35]. The resulting Rabi and Ramsey oscillations are shown in Figs. 1(g)–1(j). The vertical axis δV_{P2} determines ε, and the centers of the Rabi chevrons in Figs. 1(g) and 1(i) occur at the ε values where f_R is resonant with the transition energy. The dependence of the Rabi oscillations on ε directly reflects changes in the corresponding energy levels, providing a characteristic fingerprint for each transition.

Figure 2 shows Rabi oscillations with two distinct resonances visible in the same plot as indicated by dashed lines at the on-resonant locations. As the driving frequency is reduced from $f_R = 6.15$ to 6.00 GHz, the centers of the oscillations overlap at $\delta V_{P2} = 1$ mV. Numerical simulations of these oscillations are shown in Figs. 2(d)–2(f), using a four-level model, where two closely spaced states

make transitions to two higher states. A key feature of these two oscillations is the difference in width as a function of δV_{P2}; this behavior is reproduced in the theoretical model by different slopes for the respective energy dispersions, where a flatter slope corresponds to longer-lived oscillations [35]. The unusual merging of the resonances is reproduced in the model with a level crossing.

Figures 1 and 2 report four transitions as a function of the gate voltages defining the quantum dot. Additional Rabi
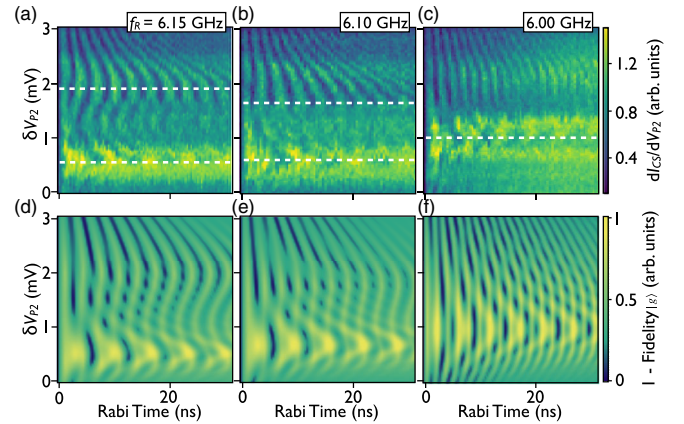
FIG. 2.   (a) Rabi oscillations with $f_R = 6.15$ GHz, with the centers of two on-resonance oscillations marked by dashed lines. (b) Rabi oscillations with $f_R = 6.10$ GHz, where the two resonances move closer together in ε as compared with (a). (c) Rabi oscillations with $f_R = 6.00$ GHz, where the on-resonance locations have completely merged. (d)–(f) Simulated Rabi oscillations corresponding to (a)–(c) using a simplified, four-level model.

oscillations were measured with microwave frequencies ranging from 3.25 to 7.6 GHz (see Sec. S4 in Supplemental Material [36]). These data demonstrate Rabi driving of eight distinct transitions below 10 GHz, an unusual density of transitions that cannot be described by noninteracting two-electron physics. We must therefore consider how electron-electron interactions influence the excited energy level spectrum [17,37,38].

A dimensionless measure of the interaction strength is $R_W = E_{ee}/E_{orb}$ [15], the ratio of the electron-electron interaction energy E_{ee} and the lowest quantum dot orbital excitation energy E_{orb}. To estimate E_{orb} we use FCI methods to diagonalize the Hamiltonian of a parabolically confined two-electron quantum dot, including the effects of valley splitting, valley-orbit coupling, and electron-electron interactions, obtaining the energy eigenvalues and eigenstates [21,39–42]. Good correspondence between theory and experiment is found with a valley splitting of 3.81 GHz and an orbital confinement energy $E_{orb}/h = 59.2$ GHz. Approximating E_{ee} as the Coulomb energy of two point charges separated by the characteristic length scale of the quantum dot, $E_{ee} = (e^2/4\pi\epsilon)\sqrt{m_t\omega_x/\hbar}$, yields $R_W = 12.7$ for a dot radius of 40 nm. This estimate is consistent with a quantum dot situated in a 90 nm wide channel below a 70 nm wide gate. Although this R_W is greater than that observed in carbon nanotubes ($R_W = 1.64$ [30]) and Ga[Al]As quantum dots ($R_W = 1.55$ [28]), recent Si-SiGe

quantum dot experiments report values of $R_W \approx 3.6$ ($E_{orb}/h = 725$ GHz [43]) and $R_W \approx 5.2$ ($E_{orb}/h = 362$ GHz [44,45]), suggesting that interactions may play an important role in many quantum dot and spin qubit experiments. Confinement energies are also suppressed in multielectron dots, which are frequently employed as qubits [2]; in such cases, we expect to observe large R_W values deep in the Wigner-molecule regime.

To understand the impact of electron-electron interactions on the two-electron energy spectrum, it is instructive to tune the Coulomb interactions in the FCI simulations by artificially introducing an effective charge e^* with $e^*/e \leq 1$, so that $R_W = (e^{*2}/4\pi\epsilon)\sqrt{m_t/\hbar^3\omega_x}$. Figure 3(a) shows the two-electron energy splittings from the ground state as e^* is changed. With increasing interaction strength, we observe that the energy eigenstates are composed of a growing number of valley and orbital basis states, and the electron positions become increasingly anticorrelated. Importantly, this hybridization results in a densely packed array of energy levels in the strong interaction regime, $e^*/e = 1$.

Figure 3(b) shows the noninteracting spectrum at $e^* = 0$ (yellow) and the fully interacting spectrum at $e^* = e$ (blue), revealing for the interacting case a manifold structure highlighted with solid and dashed boxes. Each of these manifolds contains both singlet and triplet states, all of which have similar electron densities. This similarity in
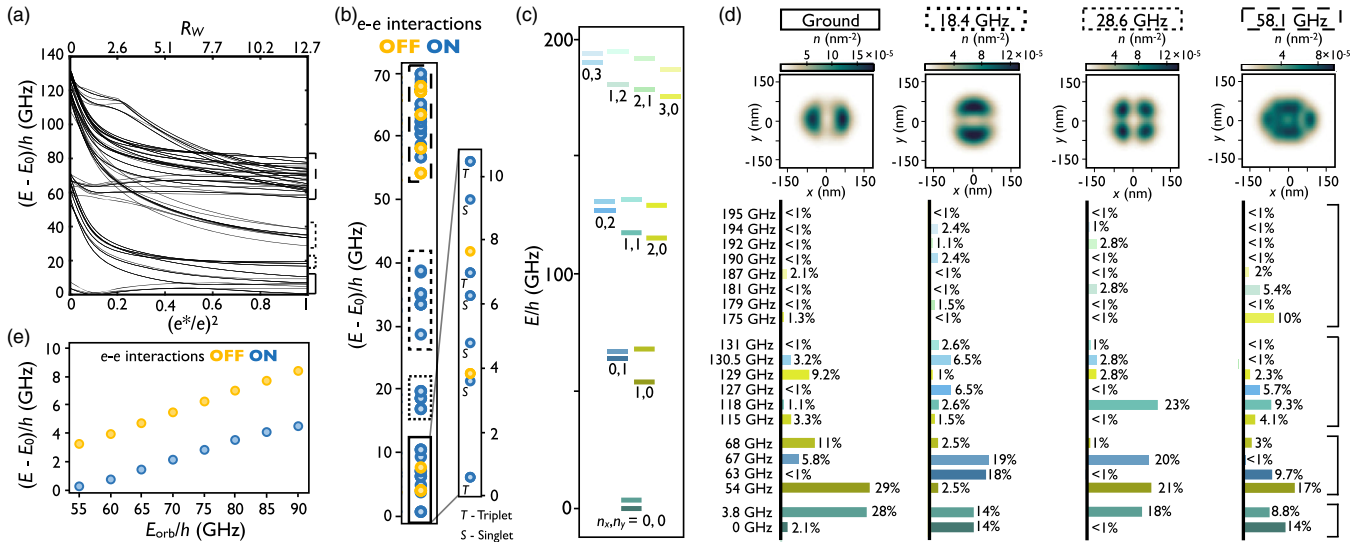

FIG. 3. FCI calculations performed using parabolic confinement potentials with $E_{orb}/h = \omega_x/2\pi = 59.2$ GHz and $\omega_y = 1.07\omega_x$. (a) Two-electron excited state energies $(E_1 - E_0)$ plotted as a function of the relative interaction strength $(e^*/e)^2$ (bottom) and the Wigner parameter R_W (top). (b) Excited state energies with ($e^* = e$, blue) and without ($e^* = 0$, yellow) interactions. The spectrum is grouped into manifolds, indicated by boxes, with the lowest manifold in the inset. (c) The single-electron energy levels used to construct the interacting two-electron wave functions in (b), with the orbitals labeled as n_x, n_y. Each grouping of orbital excitations forms a valley-split doublet. (d) Electron density distributions of the lowest-energy singlet wave functions in each of the four manifolds in (b), identified by the corresponding border style. The bar plots below indicate the contributions from each of the single-electron wave functions in (c). (e) Two-electron singlet-triplet splitting with (blue) and without (yellow) electron-electron interactions as a function of orbital confinement, demonstrating large variation as a function of E_{orb} when interactions are strong.

energy and spatial density within a manifold can be understood by looking at the corresponding combinations of single-particle basis states. These single-particle states up to 195 GHz are shown in Fig. 3(c) and consist of x and y orbital excitations (n_x, n_y) and valley state excitations. Figure 3(d) reports the in-plane electron density and the fractional contribution of the single-particle states for the first singlet level within each manifold shown in Fig. 3(b). The transitions between manifolds in Fig. 3(b) correspond to quantitative changes in the contributions of single-particle states. For example, Fig. 3(d) reveals the largest contributions to the ground state singlet are from two states: the $(n_x, n_y) = (0, 0)$ high energy valley eigenstate and the $(n_x, n_y) = (1, 0)$ low energy valley eigenstate. In the next manifold, there are roughly equal contributions from each valley eigenstate for a given single-particle state and a switch from (1,0) to (0,1). The evolution in the contributions from the single-particle orbital modes is revealed both in the bar graphs and the electron density plots.

An important characteristic of the large R_W regime is that relatively small changes in E_{orb} lead to rapid changes in the lowest-energy gap in the system (the singlet-triplet splitting). Figure 3(e) plots these theoretically calculated energy splittings with (blue) and without (yellow) electron interactions as a function of lateral confinement strength. Changing the confinement from 55 to 90 GHz (less than a factor of 2 change) in the presence of interactions results in variation of the singlet-triplet splitting by more than a factor of 20.

Figure 4 summarizes the experimental results on DQD detuning plots. Figure 4(a) shows the eigenvalues of a Hamiltonian with five uncoupled excited states in the right quantum dot, each coupled to the left quantum dot's ground state, used to fit the Rabi and Ramsey data reported in this Letter. We anticipate that both singlet and triplet spin configurations are present among these two-electron excited states based on the FCI calculations in Fig. 3. Transitions between such spin states are mediated by virtual tunneling events similar to the quantum dot hybrid qubit (QDHQ), as described in Ref. [10].

The excited state energies in the infinite-detuning limit E_1–E_5 are motivated by the energy levels reported in Fig. 3. Figure 4(b) plots in dark teal the difference in energy between the ground and excited states E_{01}–E_{05}, which depend on ε. It plots in light teal the difference between the higher excited states and the first excited state energy E_{12}–E_{15} ($E_1/h = 0.75$ GHz). Though the energy splitting E_{01} is not directly observed, its presence is motivated by the FCI calculations described above, and we infer its existence and energy from the data plotted in Fig. 4(b). We believe this state has nonzero initialization occupation because of both nonadiabaticity of the pulse sequence and thermal excitation caused by electron temperatures of about 100 mK ($k_B T = 2.1$ GHz).
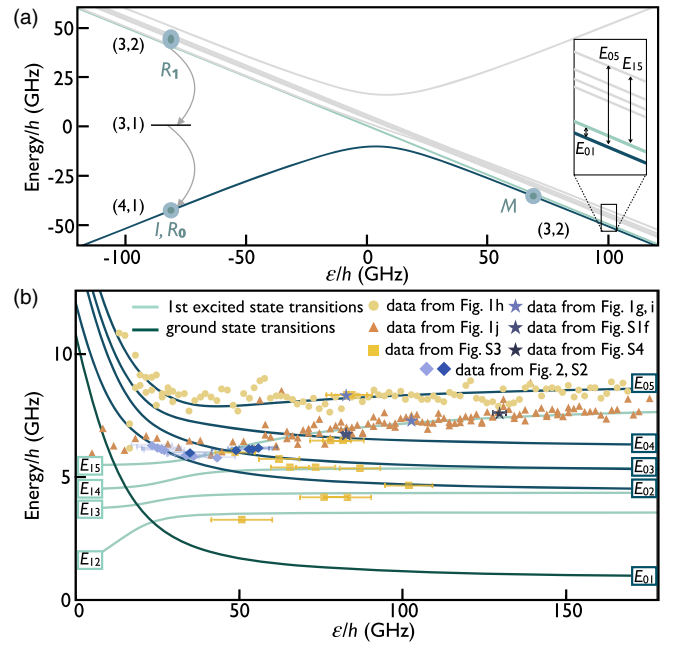

FIG. 4. (a) Energy eigenvalues versus ε of a Hamiltonian motivated by the electron interaction effects reported here. Measurement locations from Fig. 1 are indicated. Inset: excited state spectrum with example transitions shown. (b) Frequencies versus ε of the eight transitions reported here, E_{01}–E_{05}, and E_{12}–E_{15}, and E_{01} which is inferred but not directly observed. The dark teal lines are the energy differences between the ground state and energy level n, defined in (a); the light teal lines are differences between the first excited level and the same energy levels in (a). Symbols plotted correspond to frequencies extracted from the experiment, as described in the legend.

The data shown in Fig. 4(b) correspond to all the Rabi and Ramsey spectra reported in this Letter, as described in the legend. We plot the spectra from Figs. 1(h) and 1(j) as light yellow circles and orange triangles, and fit to them the transitions E_{05} and E_{15}, corresponding to the differences between the ground and first excited states to the fifth excited state. The resonant frequencies from Figs. 2(a)–2(c) that move up (down) between Figs. 2(a) and 2(c) are shown as light (navy) blue diamonds.

The merging of these points with decreasing f_R provides additional evidence that these Rabi oscillations are driven from the ground and first excited state; if these two resonances belonged to the same dispersion, they would merge into a single chevron at the dispersion minimum instead of overlapping. If both transitions occurred as excitations from the ground state, a level crossing would only occur if one of the tunnel couplings was anomalously low (≤ 0.1 GHz) which is not supported by the shape of the Ramsey spectra. Finally, the yellow squares in Fig. 4(b) show energies corresponding to Rabi oscillations with a 4.4 GHz range of microwave frequencies. The density of transitions in frequency space as compared with the FCI calculations supports the necessity to consider both E_0 and

E_1 transitions. In total, Fig. 4 summarizes the coherent control of eight transitions in this Wigner molecule, E_{02}–E_{05}, and E_{12}–E_{15}, and highlights how these transitions depend on ε.

As shown in Fig. 3(e), for large R_W, the singlet-triplet splitting becomes highly tunable, offering opportunities and pitfalls for applications in quantum dot qubits. For qubits like the QDHQ, where it is useful to tune the singlet-triplet splitting to a desired value, interactions can amplify small changes in confinement-defining gate voltages into large and useful changes in singlet-triplet splittings. However, for other qubits such as Loss-DiVincenzo, singlet-triplet, and exchange-only qubits, unexpectedly large shifts in the singlet-triplet splitting could weaken or prevent read-out mechanisms like the Pauli spin blockade. Furthermore, as seen in this Letter, a suppressed singlet-triplet splitting may be accompanied by additional low-lying energy levels, which can interfere with the two-level system required for a qubit.

In conclusion, we have studied a quantum dot in the limit of large R_W, where the electron-electron interaction energy scale surpasses the orbital energy splitting. In this regime, we identify and coherently control eight separate resonances. Based on theoretical calculations we have argued that these states arise from strong interactions and Wigner-molecule physics. We use a six-level model, motivated by both experiment and FCI calculations, to explain how the dense set of energy levels in a single dot affects the DQD spectrum as a function of ε. The observation of Wigner molecules in silicon quantum dots suggests that small changes in confinement can have a strong effect on the qubit energy splitting in this system. This could be harnessed as a tool for controlling qubit energy splittings, but if unanticipated, this phenomenon could also lead to qubit interference from low-lying levels or the suppression of level-dependent qubit readout.

The Supplemental Material [36] provides additional raw data and technical details on the models used in Fig. 2 and Fig. 4, the FCI calculations, the estimations of state populations, the experimental setup, and includes Ref. [46–48].

*Corresponding author.
 maeriksson@wisc.edu

[1] C. H. Yang, R. C. Leon, J. C. Hwang, A. Saraiva, T. Tanttu, W. Huang, J. Camirand Lemyre, K. W. Chan, K. Y. Tan, F. E. Hudson, K. M. Itoh, A. Morello, M. Pioro-Ladrière, A. Laucht, and A. S. Dzurak, Nature (London) **580**, 350 (2020).

[2] R. C. Leon, C. H. Yang, J. C. Hwang, J. C. Lemyre, T. Tanttu, W. Huang, K. W. Chan, K. Y. Tan, F. E. Hudson, K. M. Itoh, A. Morello, A. Laucht, M. Pioro-Ladrière, A. Saraiva, and A. S. Dzurak, Nat. Commun. **11**, 797 (2020).

[3] D. Kim, Z. Shi, C. B. Simmons, D. R. Ward, J. R. Prance, T. S. Koh, J. K. Gamble, D. E. Savage, M. G. Lagally, M. Friesen, S. N. Coppersmith, and M. A. Eriksson, Nature (London) **511**, 70 (2014).

[4] K. Ono, D. G. Austing, Y. Tokura, and S. Tarucha, Science **297**, 1313 (2002).

[5] J. R. Petta, A. C. Johnson, J. M. Taylor, E. A. Laird, A. Yacoby, M. D. Lukin, C. M. Marcus, M. P. Hanson, and A. C. Gossard, Science **309**, 2180 (2005).

[6] M. D. Shulman, O. E. Dial, S. P. Harvey, H. Bluhm, V. Umansky, and A. Yacoby, Science **336**, 202 (2012).

[7] M. D. Reed, B. M. Maune, R. W. Andrews, M. G. Borselli, K. Eng, M. P. Jura, A. A. Kiselev, T. D. Ladd, S. T. Merkel, I. Milosavljevic, E. J. Pritchett, M. T. Rakher, R. S. Ross, A. E. Schmitz, A. Smith, J. A. Wright, M. F. Gyure, and A. T. Hunter, Phys. Rev. Lett. **116**, 110402 (2016).

[8] L. Gaudreau, G. Granger, A. Kam, G. C. Aers, S. A. Studenikin, P. Zawadzki, M. Pioro-Ladrière, Z. R. Wasilewski, and A. S. Sachrajda, Nat. Phys. **8**, 54 (2012).

[9] J. Medford, J. Beil, J. M. Taylor, E. I. Rashba, H. Lu, A. C. Gossard, and C. M. Marcus, Phys. Rev. Lett. **111**, 050501 (2013).

[10] Z. Shi, C. B. Simmons, J. R. Prance, J. K. Gamble, T. S. Koh, Y.-P. Shim, X. Hu, D. E. Savage, M. G. Lagally, M. A. Eriksson, M. Friesen, and S. N. Coppersmith, Phys. Rev. Lett. **108**, 140503 (2012).

[11] R. Li, L. Petit, D. P. Franke, J. P. Dehollain, J. Helsen, M. Steudtner, N. K. Thomas, Z. R. Yoscovits, K. J. Singh, S. Wehner, L. M. K. Vandersypen, J. S. Clarke, and M. Veldhorst, Sci. Adv. **4**, eaar3960 (2018).

[12] L. M. K. Vandersypen, H. Bluhm, J. S. Clarke, A. S. Dzurak, R. Ishihara, A. Morello, D. J. Reilly, L. R. Schreiber, and M. Veldhorst, npj Quantum Inf. **3**, 34 (2017).

[13] L. Petit, H. G. J. Eenink, M. Russ, W. I. L. Lawrie, N. W. Hendrickx, S. G. J. Philips, J. S. Clarke, L. M. K. Vandersypen, and M. Veldhorst, Nature (London) **580**, 355 (2020).

[14] G. W. Bryant, Phys. Rev. Lett. **59**, 1140 (1987).

[15] C. Yannouleas and U. Landman, Phys. Rev. Lett. **82**, 5325 (1999).

[16] J. Cioslowski and K. Pernal, J. Chem. Phys. **113**, 8434 (2000).

[17] S. M. Reimann, M. Koskinen, and M. Manninen, Phys. Rev. B **62**, 8108 (2000).

[18] A. V. Filinov, M. Bonitz, and Y. E. Lozovik, Phys. Rev. Lett. **86**, 3851 (2001).

[19] B. Reusch, W. Häusler, and H. Grabert, Phys. Rev. B **63**, 113313 (2001).

[20] B. Szafran, F. M. Peeters, S. Bednarek, T. Chwiej, and J. Adamowski, Phys. Rev. B **70**, 035401 (2004).

[21] M. Rontani, C. Cavazzoni, D. Bellucci, and G. Goldoni, J. Chem. Phys. **124**, 124102 (2006).

[22] A. Ghosal, A. D. Güçlü, C. J. Umrigar, D. Ullmo, and H. U. Baranger, Phys. Rev. B **76**, 085341 (2007).

[23] F. Cavaliere, U. D. Giovannini, M. Sassetti, and B. Kramer, New J. Phys. **11**, 123004 (2009).

[24] I. Shapir, A. Hamo, S. Pecker, C. P. Moca, Ö. Legeza, G. Zarand, and S. Ilani, Science **364**, 870 (2019).

[25] A. M. Mintairov, J. Kapaldo, J. L. Merz, S. Rouvimov, D. V. Lebedev, N. A. Kalyuzhnyy, S. A. Mintairov, K. G. Belyaev, M. V. Rakhlin, A. A. Toropov, P. N. Brunkov, A. S. Vlasov, Y. Zadiranov, S. A. Blundell, A. M. Mozharov, I. Mukhin, M. Yakimov, S. Oktyabrsky, A. V. Shelaev, and V. A. Bykov, Phys. Rev. B **97**, 195443 (2018).

[26] S. Kalliakos, M. Rontani, V. Pellegrini, C. P. García, A. Pinczuk, G. Goldoni, E. M. ad Loren N. Pfeiffer, and K. W. West, Nat. Phys. **4**, 467 (2008).

[27] A. Singha, V. Pellegrini, A. Pinczuk, L. N. Pfeiffer, K. W. West, and M. Rontani, Phys. Rev. Lett. **104**, 246802 (2010).

[28] C. Ellenberger, T. Ihn, C. Yannouleas, U. Landman, K. Ensslin, D. Driscoll, and A. C. Gossard, Phys. Rev. Lett. **96**, 126806 (2006).

[29] L. H. Kristinsdóttir, J. C. Cremon, H. A. Nilsson, H. Q. Xu, L. Samuelson, H. Linke, A. Wacker, and S. M. Reimann, Phys. Rev. B **83**, 041101(R) (2011).

[30] S. Pecker, F. Kuemmeth, A. Secchi, M. Rontani, D. C. Ralph, P. L. McEuen, and S. Ilani, Nat. Phys. **9**, 576 (2013).

[31] D. M. Zajac, T. M. Hazard, X. Mi, K. Wang, and J. R. Petta, Appl. Phys. Lett. **106**, 223507 (2015).

[32] J. P. Dodson, N. Holman, B. Thorgrimsson, S. F. Neyens, E. R. MacQuarrie, T. McJunkin, R. H. Foote, L. F. Edge, S. N. Coppersmith, and M. A. Eriksson, Nanotechnology **31**, 505001 (2020).

[33] L. A. Tracy, D. R. Luhman, S. M. Carr, N. C. Bishop, G. A. T. Eyck, T. Pluym, J. R. Wendt, M. P. Lilly, and M. S. Carroll, Appl. Phys. Lett. **108**, 063101 (2016).

[34] S. A. Studenikin, J. Thorgrimson, G. C. Aers, A. Kam, P. Zawadzki, Z. R. Wasilewski, A. Bogan, and A. S. Sachrajda, Appl. Phys. Lett. **101**, 233101 (2012).

[35] B. Thorgrimsson, D. Kim, Y.-C. Yang, L. W. Smith, C. B. Simmons, D. R. Ward, R. H. Foote, J. Corrigan, D. E. Savage, M. G. Lagally, M. Friesen, S. N. Coppersmith, and M. A. Eriksson, npj Quantum Inf. **3**, 32 (2017).

[36] See Supplemental Material at http://link.aps.org/supplemental/10.1103/PhysRevLett.127.127701 for additional data, as well as details of theoretical simulation and explanation of analysis procedures.

[37] U. Merkt, J. Huser, and M. Wagner, Phys. Rev. B **43**, 7320 (1991).

[38] S. A. Blundell and S. Chacko, Phys. Rev. B **83**, 195444 (2011).

[39] L. Wang, K. Shen, B. Y. Sun, and M. W. Wu, Phys. Rev. B **81**, 235326 (2010).

[40] E. Wach, D. P. Zebrowski, and B. Szafran, J. Phys. Condens. Matter **25**, 335801 (2013).

[41] F. Cavaliere, N. T. Ziani, F. Negro, and M. Sassetti, J. Phys. Condens. Matter **26**, 505301 (2014).

[42] H. E. Ercan, S. N. Coppersmith, and M. Friesen, arXiv:2105.10645.

[43] D. M. Zajac, T. M. Hazard, X. Mi, E. Nielsen, and J. R. Petta, Phys. Rev. Applied **6**, 054013 (2016).

[44] A. Hollmann, T. Struck, V. Langrock, A. Schmidbauer, F. Schauer, T. Leonhardt, K. Sawano, H. Riemann, N. V. Abrosimov, D. Bougeard, and L. R. Schreiber, Phys. Rev. Applied **13**, 034068 (2020).

[45] E. H. Chen, K. Raach, A. Pan, A. A. Kiselev, E. Acuna, J. Z. Blumoff, T. Brecht, M. Choi, W. Ha, D. Hulbert, M. P. Jura, T. Keating, R. Noah, B. Sun, B. J. Thomas, M. Borselli, C. Jackson, M. T. Rakher, and R. S. Ross, Phys. Rev. Applied **15**, 044033 (2021).

[46] T. B. Boykin, G. Klimeck, M. A. Eriksson, M. Friesen, S. N. Coppersmith, P. von Allmen, F. Oyafuso, and S. Lee, Appl. Phys. Lett. **84**, 115 (2004).

[47] T. B. Boykin, G. Klimeck, M. Friesen, S. N. Coppersmith, P. vonAllmen, F. Oyafuso, and S. Lee, Phys. Rev. B **70**, 165325 (2004).

[48] R. A. Faulkner, Phys. Rev. **184**, 713 (1969).